Smart Structures and Systems, *Vol. 27, No. 1 (2021) 35-52*
DOI: https://doi.org/10.12989/sss.2021.27.1.035

Automated UAV based multi-hazard assessment system for bridges crossing seasonal rivers

Orkan Özcan*[1] and Okan Özcan [2]

[1] *Eurasia Institute of Earth Sciences, İstanbul Technical University, 34469, Istanbul, Turkey*
[2] *Department of Civil Engineering, Akdeniz University, 07058, Antalya, Turkey*

(*Received January 28, 2020, Revised November 13, 2020, Accepted November 16, 2020*)

Abstract. An automated unmanned aerial vehicle (UAV) based multi-hazard performance assessment system was developed to respond to rapid performance evaluation and performance prediction needs for river crossing reinforced concrete (RC) bridges. In the developed system, firstly the seasonally acquired UAV measurements were used to obtain the three-dimensional (3D) digital elevation models (DEMs) of the river bed. In conjunction with the flood simulation, the hydraulic model was verified with the previous flood event which corresponded to Q50 and the scour depths after a probable flood (Q500) were predicted by HEC-RAS software. Afterward, the 3D finite element model (FEM) of the bridge was constituted automatically with the developed code considering the scoured piles. The flood loads were exerted on the modeled bridge with regard to the HEC-RAS flood inundation map and relevant water depth estimations around the bridge piers. For the seismic evaluation, nonlinear time history analyses (THA) were conducted by using several scaled earthquake acceleration records that were acting in both principal axes of the bridge simultaneously as compatible with the region seismicity. The Boğaçay-II Bridge that was located in Antalya, Turkey was selected as the case study. In the analyses, as the scour depth increased, the lateral displacements and the pile internal forces were observed to increase while the pier column internal forces kept approximately constant. Thus, it was monitored that the seismic displacement and load demands migrated from pier columns to piles with increasing scour. Therefore, the applicability of the proposed system was verified using the case study bridge.

Keywords: UAV-photogrammetry; automated system; multi-hazard; bridge; scour; seismic performance; earthquake; flood

1. Introduction

The multi-hazard performance of river crossing bridges should be determined periodically due to perpetual alterations in riverbed morphology arising from natural events such as stream flow, storms, floods, and earthquakes. Thus, specifically the pile supported river bridges were expected to experience changes in the foundation system and in the accompanying relevant loads. Under particular circumstances, these changes may trigger each other and may even lead to a total collapse of the bridge such that increasing amount of flood induced scour gives rise to an increase in flood loads while simultaneously triggering scouring. Bridge scour is defined as stream flow or flood induced erosion of soil particles around bridge foundations and it can be considered as the most common cause for the failure of river bridges (Richardson *et al*. 1993). Increasing in scour depth has been found to deteriorate the lateral capacity of the foundation while maximizing the internal forces (Zaky *et al*. 2020). This phenomenon, in turn may result in bridge instability, posing a potential threat to public safety that amplifies the adverse effect of seismic ground motions and flood loads on bridge performance (AASHTO 2017). According to Lagasse *et al*. (1997), scouring was responsible for 60% of bridge failures in the United States. Wardhana and Hadipriono (2003) reported that out of 503 bridge failures in the United States, the flood and scour related cases were found to constitute 53% of all causes of failures. However, 3.38% of the failures were due to earthquakes. Similarly, Klinga and Alipour (2015) reported that scouring was the cause of approximately 50% of the failures of the bridges that overpass waterways in the United States. In Turkey, flood and flood induced scour events caused collapse or severe damage to many river crossing bridges in recent years. According to State Hydraulic Works Report (SHWR 2018), Boğaçay Bridge in Antalya was heavily damaged due to flood induced scour in 2003 that corresponded to a 50-year return period with a measured discharge of 1940 m^3/s. In 2012, Çaycuma Bridge that was located on Filyos River collapsed resulting 15 deaths for which the failure occurred due to hydraulic reasons (Yanmaz and Caner 2012). Yayakent Bridge in İzmir had a risk of collapsing due to extreme flood in 2016 (Kizilduman 2016).

Related studies on the combined effect of earthquake and scour on bridge performance was conducted and seismic fragility curves were generated (Alipour *et al*. 2010, Banerjee and Prasad 2013, Guo *et al*. 2019, Liao *et al*. 2018b, Wang *et al*. 2014, Yilmaz *et al*. 2018) with regard to assumed scour depths. It was mentioned that the scour should be taken into consideration during bridge design and evaluation since it may amplify the bridge damage via

*Corresponding author, Associate Professor,
E-mail: ozcanork@itu.edu.tr

ISSN: 1738-1584 (Print), 1738-1991 (Online)

transferring the internal forces from pier to pile while underestimating the seismic demand of the scoured piles (Klinga and Alipour 2015, Wang *et al*. 2014, 2015, Avsar *et al*. 2017, Fioklu and Alipour 2019, Ozcan and Ozcan 2018, 2019, Song *et al*. 2015). For the scour vulnerable bridges under flood induced loading, Hung and Yau (2017) proposed a safety index method in order to specify bridge performance under different scour conditions. Since the research on flood hazard fragility models were limited, Gidaris *et al*. (2017) stated the need of analytical fragility models for the bridges vulnerable to flood hazard under scour effects. Kızılduman *et al*. (2018) evaluated the multi-hazard bridge performance under flood and seismic loads by implementing the HEC-RAS software in flood and scour calculations. A risk based methodology for bridges under multiple hazards of live load, corrosion, earthquake and scour was proposed by Deco and Frangopol (2011). In order to evaluate different failure mechanisms due to earthquake, flood and ground, Gehl and D'Ayala (2016) proposed multi-hazard fragility functions. Regarding automated systems for bridge health evaluation, real time monitoring systems were provided by using wireless sensor network and global positioning system (Hu *et al*. 2013, Skibniewski *et al*. 2014). The use of UAV based methods for bridge inspection have been recently shown to improve the adoption of nondestructive bridge evaluation technologies (Liu *et al*. 2014, Dorafshan and Maguire 2018, Duque *et al*. 2018, Jung *et al*. 2019). Herein, UAVs were used to inspect the defects on bridge components (Ellenberg *et al*. 2016, Escobar-Wolf *et al*. 2018, Hada *et al*. 2017, Ikeda *et al*. 2019, Lei *et al*. 2018, Lee *et al*. 2019, Metni and Hamel 2017, Omar and Nehdi 2017, Salaan *et al*. 2018, Sanchez-Cuevas *et al*. 2019, Seo *et al*. 2018), to evaluate the resulting condition of the bridges through three-dimensional (3D) reconstructions (Lei *et al*. 2018, Lee *et al*. 2019, Cali and Ambu 2018, Chen *et al*. 2019, Hackl *et al*. 2018, Khaloo *et al*. 2018, Kim *et al*. 2018, Pan *et al*. 2019) or to capture the bridge characteristics (Hoskere *et al*. 2019). Besides, UAV generated point clouds were used to obtain the digital elevation models (DEMs) of the rivers along which the bridges were located by using Structure from Motion (SfM) algorithm (Ozcan and Ozcan 2018, 2019, Coveney and Roberts 2017, Flener *et al*. 2013, Hemmelder *et al*. 2018, Izumida *et al*. 2017, Javernick *et al*. 2014, Langhammer 2018, Schumann *et al*. 2019, Villanueva *et al*. 2019, Watanabe and Kawahara 2016) and relevant hydraulic analyses were conducted based on flood/scouring by using the HEC-RAS software (Kizilduman *et al*. 2018, Czech *et al*. 2016, Goncalves *et al*. 2015, Liao *et al*. 2018a, Muthusamy *et al*. 2019, Patel *et al*. 2017). Hence, in order to determine the multi-hazard performance of the river crossing bridges located in seismically active and flood-prone regions, quick and automated assessment strategies should be pursued as an integral part of continuous bridge health monitoring systems. Therefore, the objective of this study was to develop an automated UAV-based multi-hazard assessment strategy for river-crossing bridges. The proposed UAV-based methodology can be conveniently and rapidly implemented in the regions in which numerous bridges crossing the same river while minimizing the time spent for modeling, evaluation and analysis. The Boğaçay-II Bridge that crosses Boğaçay River located in Antalya, Turkey was selected as the case study. For this pile-supported reinforced concrete (RC) bridge, the current multi-hazard performance under existing scour conditions (corr. to Q_{50}) and the predicted performance under estimated scour depths (acc. to Q_{500}) was determined under both seismic excitations and flood loading. The analyses were conducted by addressing the sub-objectives of: (a) to examine the effect of scour on seismic behavior of the bridge, (b) to observe the effect of scour on pile load and shear capacity by nonlinear time history analyses (THA), and (c) to evaluate the performance of scoured bridge under flood loading with predicted scour.

2. Method

The followed procedure for the proposed multi-hazard bridge assessment system is presented in the flowchart given in Fig. 1. As shown, four main procedures were defined namely; (a) UAV derived DEM generation regarding seasonal flights via 3D reconstruction by using Structure from Motion algorithm (SfM), (b) hydraulic analyses by means of flood induced scour analyses and flood load/scour depth estimation by HEC-RAS 2D hydraulic modeling, (c) automated 3D FEM generation for the inspected bridge by SAP2000 (2018), and (d) multi-hazard assessment methods via flood loading and earthquake excitations. The sub-procedures were defined in the flowchart while obtaining the DEM, 3D FEM, conducting hydraulic analyses, and evaluating the multi-hazard performance for the bridge (i.e., UAV imagery processing details, soil property definitions, flood analysis details, scour depth analysis, and THA).

2.1 UAV-derived DEM generation by 3D reconstruction

The implemented methodology to generate high-resolution DEM encapsulated point cloud generation process via UAV derived aerial photos in which the SfM technique was used instead of traditional survey methods. Pix4D photogrammetric software was used to implement SfM algorithm. Herein, the 3D structural models of terrain, buildings, and landforms were obtained by motion-integrated two-dimensional (2D) image clusters by simultaneous solution using model geometry, camera position, and orientation data. As the remotely sensed object features such as edges and corners were tracked in between the imageries, relationship between the imageries was identified, and the object 3D location was determined by the feature trajectories that implied the followed route of that object (Javernick *et al*. 2014). For the regions having different geomorphic characteristics, high measurement accuracies were acquired by the SfM technique along with UAV derived imageries (Hackl *et al*. 2018, Javernick *et al*. 2014, Castillo *et al*. 2012, James and Robson 2012).

In the study region, the DEM of the river basin was acquired by DJI Mavic Pro (1/2.3" CMOS sensor with a total

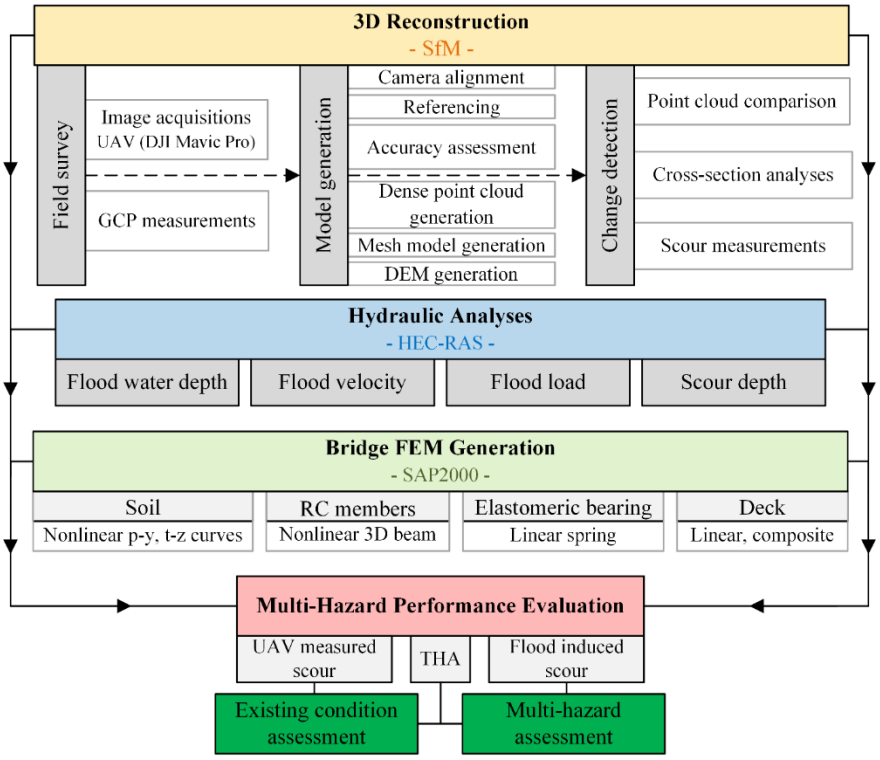

Fig. 1 Flowchart of the proposed bridge multi-hazard assessment system

pixel count of 12.71 M, capturing photos at 4000 × 3000 pixels. The lens is a 28 mm focal length with 78.8° field of view at f/2.2) via 152 ground control points (GCPs) taken along the river region (stream channel area of approx. 18 km^2) and along the inspected bridge during the UAV flights with real-time kinematic (RTK) GPS measurements during the field survey. In model generation, after camera alignment and referencing, the obtained accuracy in the generated point cloud was assessed. The average planimetric and altimetric accuracies were obtained as 0.050 and 0.080 m, respectively. In order to obtain the 3D surfaces in the riverbed and bridge regions with high accuracy, an average flight altitude was fixed at 70 meters, the overlapping ratios for both the frontal and lateral directions were optimized as 85%, and an average ground sampling distance (GSD) of 1−2 cm/pixel was ensured. Moreover, the scour depth under bridge piers was derived by manual designation of the flight heights with varying camera angles between 45- and 55-degrees nadir-off angles. Upon the generation of the dense point cloud, the DEM of the riverbed was generated subsequent to mesh model generation. In order to track the changes in riverbed morphology, change detection analyses were conducted by means of point cloud comparison by ESRI ArcGIS AddIn-Geomorphic Change Detection Tool GCD v7.2.

Herein, the scour depths around bridge piers and piles were measured using the acquired high-resolution orthophotos and dense point clouds by obtaining several lateral and longitudinal cross sections along the riverbed close to the inspected bridge. The scour depths monitored at the bridge piers were considered as input data in bridge substructure 3D FEM. It should be noted that the aforementioned UAV based measurement procedures are valid and give meaningful results only for shallow river systems in which the riverbed is dry during most of the year. Therefore, the measurements related to the bridges located on deep water rivers fall outside the scope of this study.

2.2 Hydraulic analyses

The generated DEM of the river basin was directly implemented in the HEC-RAS software (US Army Corps of Engineers Institute for Water Resources Hydraulic Engineering Center, Davis, California), which was developed for 2D hydrodynamic analyses of the rivers with multi-way and non-prismatic cross sections for flood water depth, flood velocity, flood load, and relevant scour depth estimations. In the hydraulic analyses, the maximum discharge was obtained by Hydrologic Engineering Center's Hydrologic Modeling System (HEC-HMS) rainfall – runoff model for the region. For the rivers at where the stream gauge network was inadequate and the intervals of temporal records were inconsistent, the Tropical Rainfall Measurement Mission (TRMM) satellite can be used in order to follow the rainfall – runoff changes which was developed to provide real time and high resolution rainfall data in tropic and sub-tropics (Wilheit 2003). Herein, since there is no nearby gauging station, the rainfall data was acquired by using the daily data obtained from the TRMM satellite (Wilheit 2003, Ozcan and Musaoglu 2017). The land use and land cover (LULC) data was obtained by UAV derived orthophotos to determine the manning coefficients.

2.3 3D FEM generation

The RC bridge 3D FEM was generated using SAP2000

(2018) software incorporating substructure components concerning the UAV scour depth measurements and HEC-RAS scour depth predictions for the bridge piles. The RC members such as the piers and the piles were modeled with nonlinear 3D beam elements and linear springs were defined for elastomeric bearings. The composite deck was modeled as a linear element concerning the project drawings. Thus, an input file was generated using MATLAB instead of defining the bridge members and soil spring properties manually in SAP2000 software (Fig. 1).

2.3.1 Soil modeling

In the generated code for the input file, the number, thickness, type, characteristic properties, and number of segments of each soil layer were used as the main parameters regarding the soil. In order to incorporate soil structure interaction (SSI), the soil deposits surrounding the substructure components (i.e., pier columns, abutments and piles) were characterized by lateral and vertical bidirectional nonlinear spring elements by means of p−y and t−z curves, respectively (Fig. 1). Herein, the height of the water table, soil type, and relative height of the soil layer to the ground surface were the preliminary parameters that designated the curve characteristics at a specified depth regarding sand (Reese *et al*. 1974, Wang and Reese 1993) and limestone (McWay and Niraula 2004, Niraula 2004) layers. For layered soil deposits, each soil layer was divided into several soil segments along which the nonlinear soil spring properties were assumed constant. Since the soil spring properties were defined with respect to the difference between the mid height of the soil segment and the ground surface, the soil spring properties were calculated according to the new ground level after scouring. In order for compatibility and direct assignment of soil spring properties to the bridge components, the piles and other buried parts of the substructure were modeled to have identical number of segments as similar to the soil layers. The lateral spring properties, which were defined at the mid height of each soil segment, were calculated by multiplying the ordinates of the p-y curves (i.e., p values) by the height of the pile segment under consideration. Similarly, t-z curve characteristics were assigned to the mid height of the pile segments after the specified vertical unit resistances were multiplied by the surface area of the pile segment. Thereby, the lateral and vertical resistance provided by each soil segment was assigned to the corresponding pile segment by means of bidirectional and nonlinear spring elements. The same process was applied to the bridge piers and abutments that were embedded wholly or partially into the soil. Since the p-y curves were generated in both longitudinal and transverse directions for the abutments, the influence of passive or active earth pressures was ignored. The input file used the outputs of seasonally measured scour depths or calculated flood induced scour depths in order to arrange the soil spring assignments along the piles. Herein, the soil spring assignments (p-y and t-z curves) were not considered for the scoured regions of the piles. Therefore, the soil spring properties were recalculated and assigned to the pile segments below the scour depth according to the parameters of new ground level, soil type, and relative height to ground level after scouring. Further, the adverse effect of frequently aligned piles on lateral resistance of pile groups was captured via p-multipliers that signified the deterioration of lateral soil resistance considering the shadowing effect in pile groups. For the piles and piers with a net spacing lower than three pile diameters, group effect was considered by using p-multipliers as per AASHTO (2014). Herein, the p components, which defined the lateral resistance for p−y curves, were multiplied by p-multipliers that were defined as 0.70, 0.50 and 0.35 for leading, second and remaining pile rows, respectively (AASHTO 2014). The same methodology was followed for the frequently aligned pier columns.

2.3.2 RC bridge modeling

All bridge members including the deck (slab and supporting girders), elastomeric bearings, pier caps, piers, abutments, pile caps, and piles were defined by the generated code. The piles, pier columns, pier caps and the simply supported girders, which were seated on elastomeric bearings, were modelled as 3D beam elements. Further, the elastomeric bearings were idealized as link elements while providing axial and shear stiffness. However, the lateral movements were prevented due to the presence of the RC shear keys between the girders. The RC bridge deck that included RC slab and equally spaced prestressed concrete (PC) girders was modelled as a linear 3D beam element having the identical properties with the composite superstructure regarding cross section area, moment of inertia, weight, and mass. Besides, longitudinally arranged gap elements that were defined at the end of each girder represented the spacing between two consecutive girders at abutments and piers. After closing of the specified gap length, very high stiffness was assumed due to girder pounding. The pile caps were modeled by rigid beam elements while ensuring rigid connection between piers (or abutments) and piles. Within this regard, the pile caps were decomposed into the rigid pier column and pile segments that were defined above and below the mid-height of the pile cap, respectively. Thus, the soil spring properties were characterized by pier properties above the pile cap mid height and pile properties were considered for the remaining parts.

Considering the member inelastic properties, plastic hinges were defined at the ends of pier columns and abutments at where the maximum bending moments occurred under lateral loads such as flood and earthquake loading. For piles, the pile cap connection was considered as one of the plastic hinge regions. However, the probable locations of all other hinges were determined by continuous tracking of the maximum bending moment region along the pile length by conducting successive pushover analyses in longitudinal and transverse directions. Herein, the effective stiffness for all RC members was used as half of the gross stiffness other than the PC girders in the pushover analyses (AASHTO 2014). The lateral load and curvature capacity of the plastic hinges were identified by conducting standard section analyses considering the orientation of the RC members along the bridge and the axial load range that was experienced during the pushover analyses. For each axial load level and relevant orientation angle of the member, the obtained moment – curvature diagram was bi-linearized to

be directly implemented in plastic hinge definitions. The plastic hinge lengths were considered equal to the depth of the cross-sections for simplicity.

2.4 Performance evaluation

After the 3D FEM generation, the acquired outputs of UAV measured seasonal scour depths were used to track the seasonal performance of the bridge under seismic loading. However, after hydraulic analyses, water depth and corresponding scour depth estimations during a probable flood were used to evaluate the bridge multi-hazard performance under flood loading and following earthquake excitations compatible with the region seismicity and geotechnical conditions of the site.

2.4.1 Flood assessment

The flood loads acting on the submerged bridge deck were determined according to FHWA (2009) regarding the main parameters of free stream velocity (v), inundation ratio (h^*), water density (ρ), and deck dimensions ($W, L,$ and s for deck width, length and height, respectively) as shown in Fig. 2(a).

The inundation ratio was defined as the height difference between free surface during flood (h_u) and the lower chord of the bridge deck (h_b) divided by the deck height (s) including the parapets (Eq. (1)).

$$h^* = \frac{h_u\text{-}h_b}{s} \tag{1}$$

Higher inundation ratio values imply more submersion of the bridge. The stream velocity and the expected water level after a flood event were obtained after the hydraulic analyses. In FHWA (2009), three force types were defined acting on inundated bridge deck namely; (a) the drag force, F_D, acting parallel to the flow while pushing the bridge off its piers and abutments, (b) the lift force, F_L, acting vertically to the flow which can lift the bridge deck off its piers and abutments, and (c) unevenly distributed forces on the bridge deck while leading to moments about center of gravity of the deck, M_{cg}, which can cause the bridge to overturn (Eqs. (2)-(4) and Fig. 2(b)). The inundation ratio based coefficients of drag (C_D), lift (C_L), and moment (C_M) were defined depending on the number of girders constituting the deck (FHWA 2009).

$$F_D = C_D \begin{cases} 0.5\rho v^2 Ls & h^* \geq 1 \\ 0.5\rho v^2 L(h_u\text{-}h_b) & h^* < 1 \end{cases} \tag{2}$$

$$F_L = C_L(0.5\rho v^2 LW) \tag{3}$$

$$M_{cg} = C_M\left(0.5\rho v^2 LW^2\right) \tag{4}$$

After the hydraulic analyses, the calculated parameters of flood water depth and flood water velocity were used to determine the flood loads in the generated input file. The flood loads were calculated by multiplying the assumed inverted triangular pressure distribution along the depth with the surface area of the bridge deck and the scoured regions while considering inundation.

2.4.2 Seismic assessment

In seismic assessment, nonlinear THA was conducted using the 3D FEM of the bridge in which the nonlinear and inelastic load deformation characteristics of the bridge members were directly incorporated. The bridge was subjected to eleven lateral earthquake excitations represented by ground motion acceleration histories that were selected from the Pacific Earthquake Engineering Research Center ground motion database (PEER 2015) as compatible with the location of the bridge with respect to the nearest faults, fault mechanisms, and site-specific geotechnical characteristics of the site (ASCE 2016). Accordingly, the records were amplitude scaled such that the average of the maximum direction spectra of the suite would not fall below 90% of the target elastic design spectrum over the period range between $0.2T_1$-$2T_1$. The target spectrum was defined as the 5% damped elastic design spectrum for the site that was obtained according to the Turkish Earthquake Code (TEC 2018). Herein, T_1 denotes the first fundamental period of the bridge. Scaled acceleration records were imposed simultaneously in longitudinal and transverse directions of the bridge.

3. The case study

3.1 Boğaçay II bridge

For the case study, the Boğaçay-II Bridge crossing the Boğaçay River in Antalya Province, Turkey was selected since this bridge was subjected to flood and stream induced scour in the recent years. The 13-span bridge under investigation had a total span length of 264.5 m with equispaced piers at 20.3 m and two abutments located at 20.60 m apart from the last piers (Figs. 3(a) and (b)). Regarding the superstructure, the deck included 22 cm thick RC slab which was supported by eight PC girders laterally

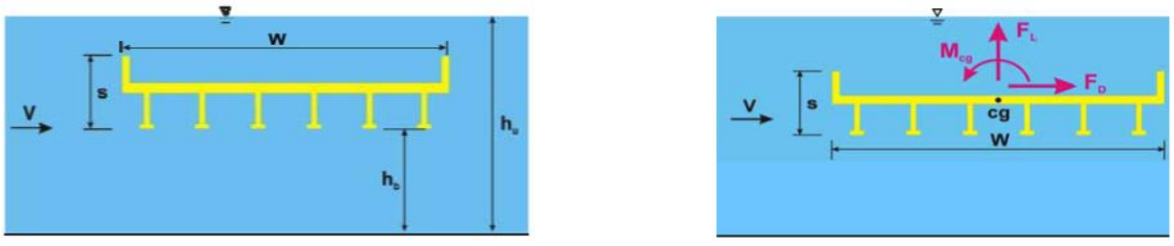

(a) (b)

Fig. 2 (a) The defined parameters; and (b) the forces and the moments for the inundated bridge deck (FHWA 2009)

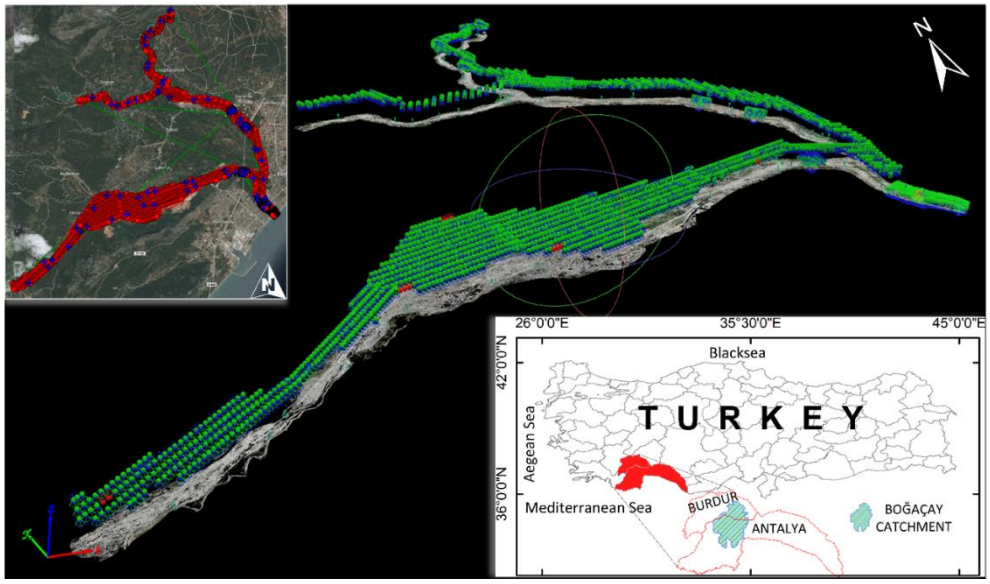

(a)

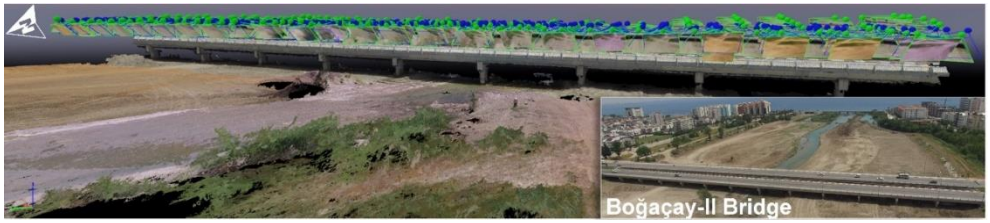

(b)

Fig. 3 (a) The location of the Boğaçay II Bridge showing Boğaçay River (approx. 18 km^2) and UAV image (1969 calibrated images) locations (red) with 152 GCPs (blue) and (b) the SfM-derived dense point cloud with top view elevation model of the bridge and the riverbed

equispaced at 1.70 m at each singly supported span. During field inspection, the gap between two consecutive girders in the longitudinal direction was determined as approximately 25 mm. As obtained from the design drawings, Grade 60 steel was used for longitudinal and transverse reinforcement with nominal yield and ultimate strength of 420 and 620 MPa, respectively. Besides, the 28 day concrete compressive strength for the PC girders and the deck slab was 40 and 25 MPa, respectively. The deck was supported by 60-durometer elastomeric bearings, which were placed at each end of the PC girders with dimensions of 250 × 450 × 95 mm (width × depth × height).

Thus, the shear modulus and consequent shear stiffness of the bearing was calculated as 1.38 MPa and 1634.2 N/mm, respectively. At each pier, three 4.5 m long pier columns (1 × 2 m) were connected to the pier cap (1.2 × 1.1 m) and the weak bending axis of the pier columns coincided with the bridge transverse axis. The center-to-center spacing between the three pier columns was 5.25 m in the transverse direction. All columns had longitudinal reinforcement of 40ϕ26 and transverse reinforcement of 10 mm diameter interlocking ties with a spacing of 100 mm. The abutments had cross-section dimensions of 1.2 × 14 m with longitudinal reinforcement of 192ϕ16 deformed rebars and 10 mm diameter stirrups spaced at 100 mm. At the bottom of each pier and abutment, a pile cap with dimensions of 3 × 14 × 1.5 m was provided to connect ten piles of 1 m diameter and 12 m long. The RC piles were spaced at 2.7 m and 3.0 m in longitudinal and transverse directions, respectively. All the piles were identically reinforced with 16ϕ26 deformed rebars and 10 mm diameter spirals with 100 mm pitch. The soil layer information was obtained by the geotechnical data presented in project drawings, and an almost homogeneous soil layer decomposition was identified among all the piers. Herein, the sand layers were observed at different heights above the pile cap and following soil layers comprised approximately 5 m limestone underlain by sand. For a reliable FEM generation, the seasonally measured topmost sand layers and the following limestone and sand layers were divided into two and five sub layers, respectively.

3.2 Results

3.2.1 UAV based scour depth measurements

For the case study bridge, firstly the high-resolution UAV imageries and incorporating GCPs taken along the river and the bridge were used to obtain the DEM of the river basin via the SfM-derived point clouds and top view elevation model (Fig. 3(b)). The seasonal changes in scour depths along the bridge piers were tracked among eleven UAV flights between October 2016 and February 2019. By using the seasonal UAV orthophotos for the inspected bridge (Figs. 4(a)-(k)), the profiles were obtained along and across the bridge (Figs. 5(a) and (b), respectively).

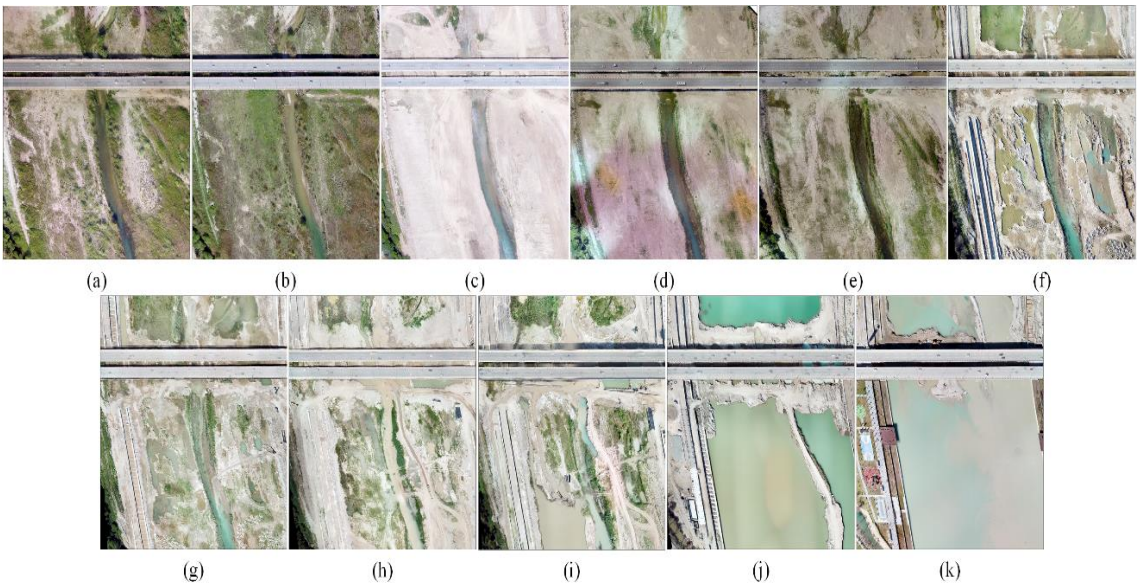

Fig. 4 Seasonal UAV imageries taken between (a)-(k) October 2016 and February 2019

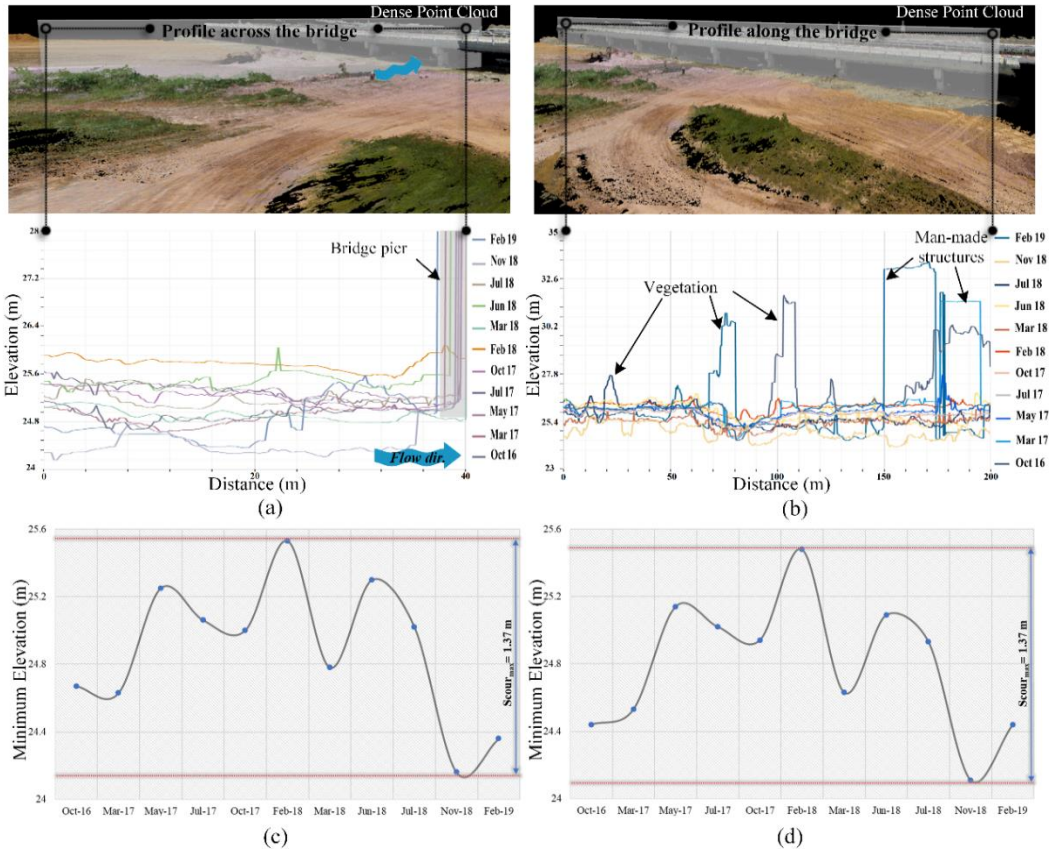

Fig. 5 The seasonal change of the profiles obtained (a) along and (b) across the bridge with the minimum elevation in profiles obtained (c) along and (d) across the bridge

The profile along the bridge was taken as close as possible to the bridge piers in order for better scour depth measurement accuracy. Herein, by comparing the seasonal scour depths from the profiles taken along the bridge in Fig. 5(a), the pier with the maximum scour depth was selected for the location at where the profile taken across the bridge was obtained (Fig. 5(b)). The spikes observed in the profiles were due to the bridge piers and man-made structures at the locations close to the bridge and due to seasonal changes in vegetation on the riverbed. After removal of the spikes, the relative changes in seasonal scour measurements were tracked by using the minimum elevations (Figs. 5(c) and (d) that indicated maxima/minima with a return period of approximately nine months (May – February for the

maxima and March – November for the minima). As shown in Fig. 5(a), scouring was significant close to the middle piers with a maximum of 1.37 m at where the seasonal river stream was concentrated by the majority.

3.2.2 Scour depth and flood load calculations by hydraulic modeling

Before hydraulic modeling, the boundary of the Boğaçay River basin was extracted by using TanDEM-X (TerraSAR-X add-on for Digital Elevation Measurement) digital elevation data with a spatial resolution of 12 m (Fig. 6(a)). Herein, the identification of flow directions and the flow accumulation regions revealed the flow network, the sub basin boundaries, and the adjoint basins by which the basin boundaries were attained (Fig. 6(b)). The daily TRMM rainfall data was specified for each grid with a spatial resolution of 0.25 degrees (approx. 25 km) in latitude and longitude, and it was associated to its corresponding region in the basin boundaries that included the entire UAV measured region in the Boğaçay River basin. For flood analyses, the daily average rainfall time series were obtained from TRMM satellite between the years 1998 and 2019 within the TRMM grid that represented the study region (Fig. 6(c)). In order to give more spatial detail in the floodplain and to fully represent all of the basin area in the model, the UAV-derived surface models were combined with resampled TanDEM-X digital surface model to be used in HEC-RAS 2D hydraulic modeling (Fig. 7(a)).

Using the daily rainfall data (Fig. 6(c)), a part of the generated 2D hydraulic model at the study region and the calculated water depths (approx. 5.0 m) along the inspected bridge close to the river mouth are shown in Figs. 7(a) and (b), respectively. The velocity vectors around the bridge piers (approx. maximum of 4.0 m/s) were used to attain the flood loads along the bridge (Fig. 7(c)). The accuracy of the generated DEM was verified regarding the previous flood event occurred in the study region with a maximum runoff of 1940 m^3/s that corresponded to a flood event with a return period of approximately 50 years (Q_{50}) (SHWR 2018). Herein, the observed elevation difference between the flood water height and the bottom of the girders appeared to be approximately 0.6 m (when it was considered that the pier cap height was 1.2 m) and a very

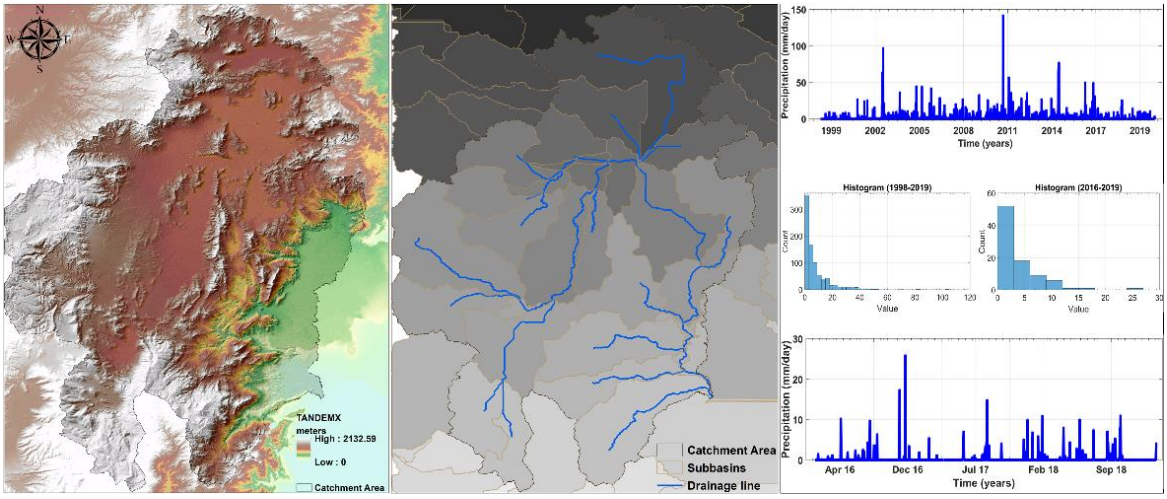

(a) (b) (c)

Fig. 6 (a) TanDEM-X digital elevation data; (b) drainage lines with the sub basins; and (c) TRMM daily average rainfall data between 1998 and 2019, (red dot indicates the bridge location)

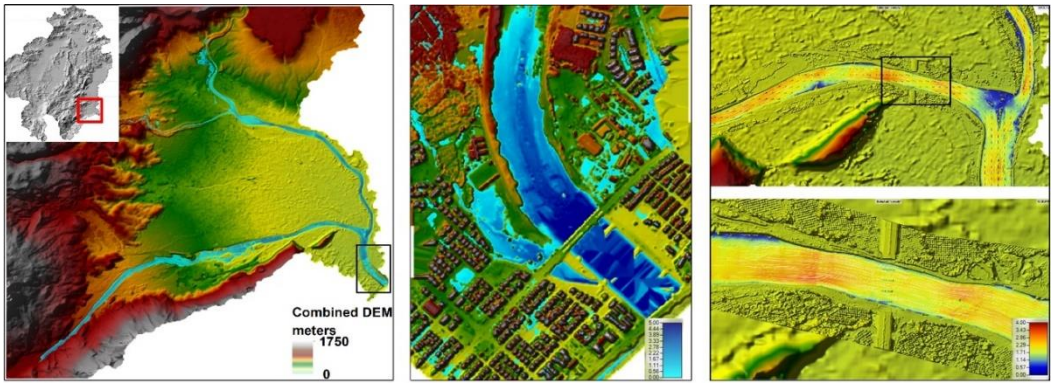

(a) (b) (c)

Fig. 7 (a) 2D hydraulic model of the study region; (b) calculated water depths along the bridge close to the river mouth; and (c) the velocity vectors obtained around the bridge by HEC-RAS

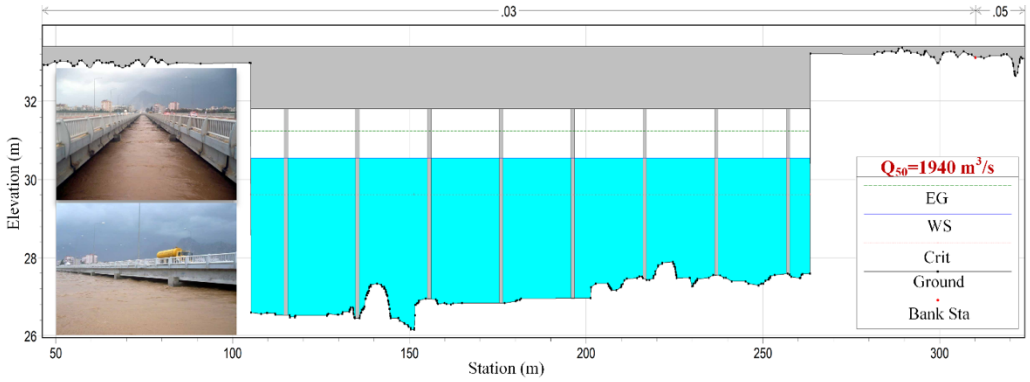

(a) (b)

Fig. 8 (a) Photos of the investigated bridge; and (b) HEC-RAS flood analysis results indicating the previous flood event in 2003

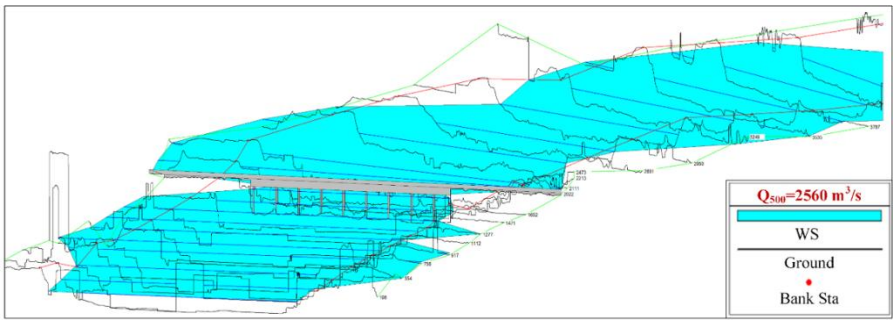

(a)

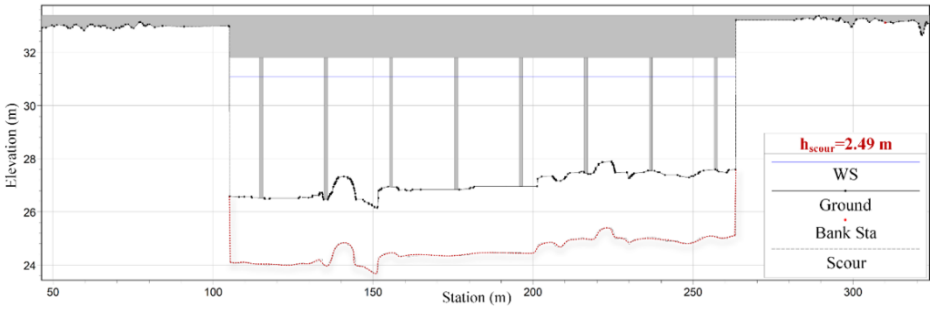

(b)

Fig. 9 HEC-RAS analysis results indicating (a) the obtained cross sections and the bridge location under the maximum runoff; and (b) the scour depths

close result was obtained in the HEC-RAS flood analysis (Figs. 8(a) and (b)). After the verification of the DEM by the flood analysis, the flood analysis was conducted for a maximum runoff of 2560 m^3/s with a calculated return period of 500 years (Q_{500}).

For this case, the obtained cross sections along the river and the location of the bridge is shown in Fig. 9(a). The results of HEC-RAS flood and scour analyses indicated that a maximum scour depth of 2.49 m (Fig. 9(b)) could be expected during a probable flood with a maximum water depth of 8.2 m measured from the scoured depth. This water level corresponded to a 0.46 m of submersion of the bridge deck since the pier height was 5.25 m and the maximum flood velocity was predicted as 5.7 m/s. The flood loads were calculated accordingly by the Eqs. (1)-(4).

3.2.3 Current and multi-hazard bridge performance assessment

In order to assess the current performance of the bridge, the investigated bridge was subjected to THA after the nonlinear dead load case with the selected and scaled suite of the ground motion records with the target spectrum (Table 1, Fig. 10).

Herein, the seasonal UAV based scour depth measurements were used while generating the bridge FEM in which the measured scour depths (i.e., maximum of 1.37 m) at each pile/pier were used in modeling and in assigning the corresponding soil properties by means of p-y and t-z curves (Figs. 11(a) and (b)). For multi-hazard assessment, the bridge was exposed to THA after considering nonlinear loading history due to subsequent flood and dead load cases. For this case, the bridge FEM was generated by using

Table 1 Ground motion suite

Earthquake	Station	M_w	R_{JB}	V_{S30}	Comp.	PGA	PGV	PGD	Scale factor
			km	*m/s*		*g*	*cm/s*	*cm*	
Imp. Val. 06	Chihuahua	6.5	7.3	242	012	0.270	24.8	9.3	2.25
					282	0.254	29.9	7.7	
Imp. Val. 06	El Cent.Arr.#11	6.5	12.6	196	140	0.365	36.0	25.1	1.89
					230	0.380	44.6	21.3	
Imp. Val. 06	El Cent.Diff.Arr.	6.5	5.1	202	270	0.352	75.5	57.1	1.37
					360	0.481	40.9	16.4	
Superst.Hills 02	El Cent.Imp.Co.	6.5	18.2	192	000	0.357	48.0	19.3	1.90
					090	0.260	41.8	21.9	
Superst.Hills 02	Poe Road	6.5	11.2	317	270	0.475	41.2	7.7	1.96
					360	0.286	29.0	11.4	
Superst.Hills 02	Westm.Fire Sta.	6.5	13.0	194	090	0.173	23.5	15.0	2.33
					180	0.211	32.3	22.3	
Landers	Coolwater	7.3	19.7	353	000	0.283	27.6	18.2	1.73
					090	0.417	43.4	15.2	
Kobe	Amagasaki	6.9	11.3	256	000	0.276	33.6	26.6	1.38
					090	0.327	44.8	23.8	
Kobe	Tadoka	6.9	31.7	312	000	0.296	24.5	7.6	2.96
					090	0.194	14.7	10.3	
Kocaeli	Duzce	7.5	13.6	282	180	0.312	58.8	44.0	1.32
					270	0.364	56.6	25.0	
Duzce	Bolu	7.1	12.0	294	000	0.739	55.9	25.6	0.94
					090	0.806	65.9	13.1	

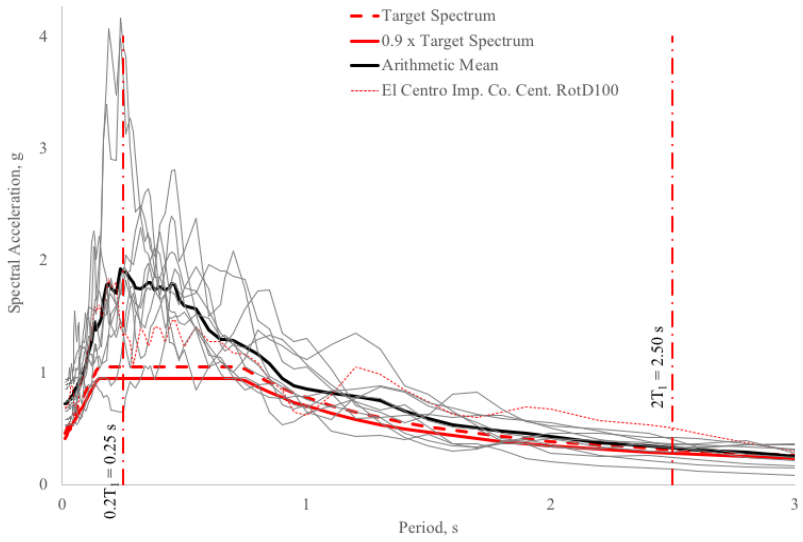

Fig. 10 RotD100 spectrum of the scaled suite, the selected record, and the target spectrum

the maximum scour depth outputs (i.e., maximum of 2.49 m for all piers) that were obtained by HEC-RAS scour analysis. Herein, 2.49 m of flood induced scour depth was defined for all piers in FEM generation while removing the soil springs at the scoured pile locations as similar to the current condition (Figs. 11(a) and (b)).

The performance of the bridge under current and multi-hazard conditions was evaluated by longitudinal and transverse displacements that were obtained at the upper ends of the pier columns for each scaled ground motion record (Figs. 12(a) and (b)). In addition, shear forces (V_x and V_y acting in x and y axes) and bending moments (M_x

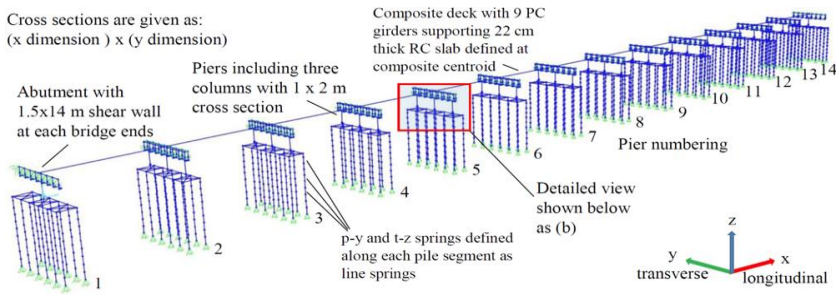

(a)

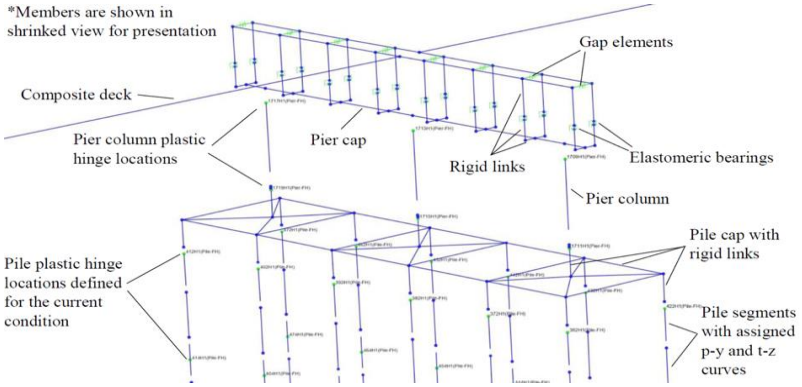

(b)

Fig. 11 (a) Boğaçay-II Bridge FEM representing plastic hinge locations; and (b) detailed view of a typical pier with gap, elastomer, and plastic hinges for a defined scour depth of 1.37 m

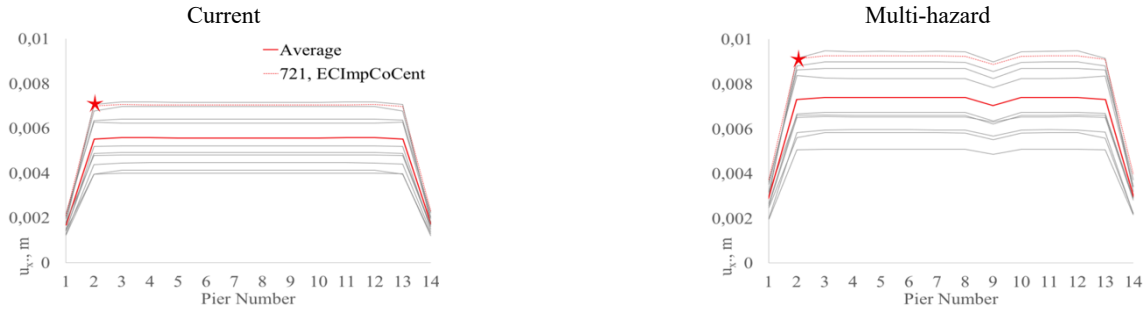

(a) Displacement in x direction (longitudinal)

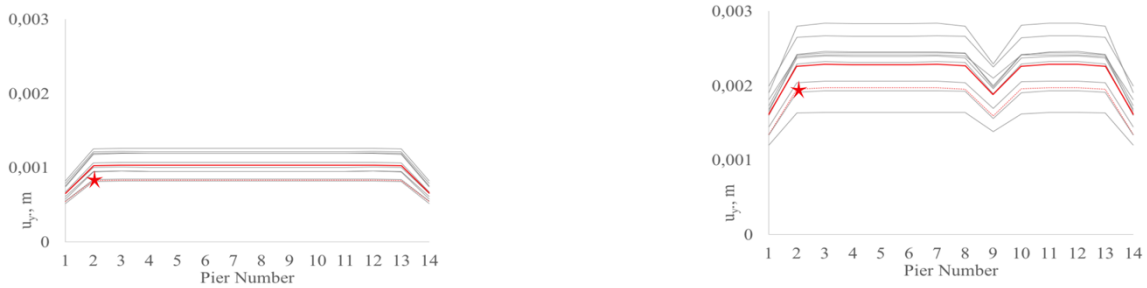

(b) Displacement in y direction (transverse)

Fig. 12 The max. pier column displacement at the upper ends for current and multi-hazard conditions

and M_y acting about x and y axes) at the pier columns and piles (Figs. 13(a)-(d) and Figs. 14(a)-(d)) were determined for evaluation and comparison. The bridge members exhibited linear elastic response under flood loading. Regarding the multi-hazard condition, the displacement demand (u_x and u_y) increased in both directions and it approximately doubled in the transverse direction (y) as compared to the current condition of the bridge (Figs. 12(a) and (b)). For the pier columns, the flood induced scour was shown to have an insignificant effect on the internal forces (Figs. 13(a)-(d)). However, the shear forces in the transverse direction (V_y) was observed to have a slight increase approximately from 1600 to 2200 kN as shown in Fig. 13(b). The moments about the longitudinal axis (i.e.,

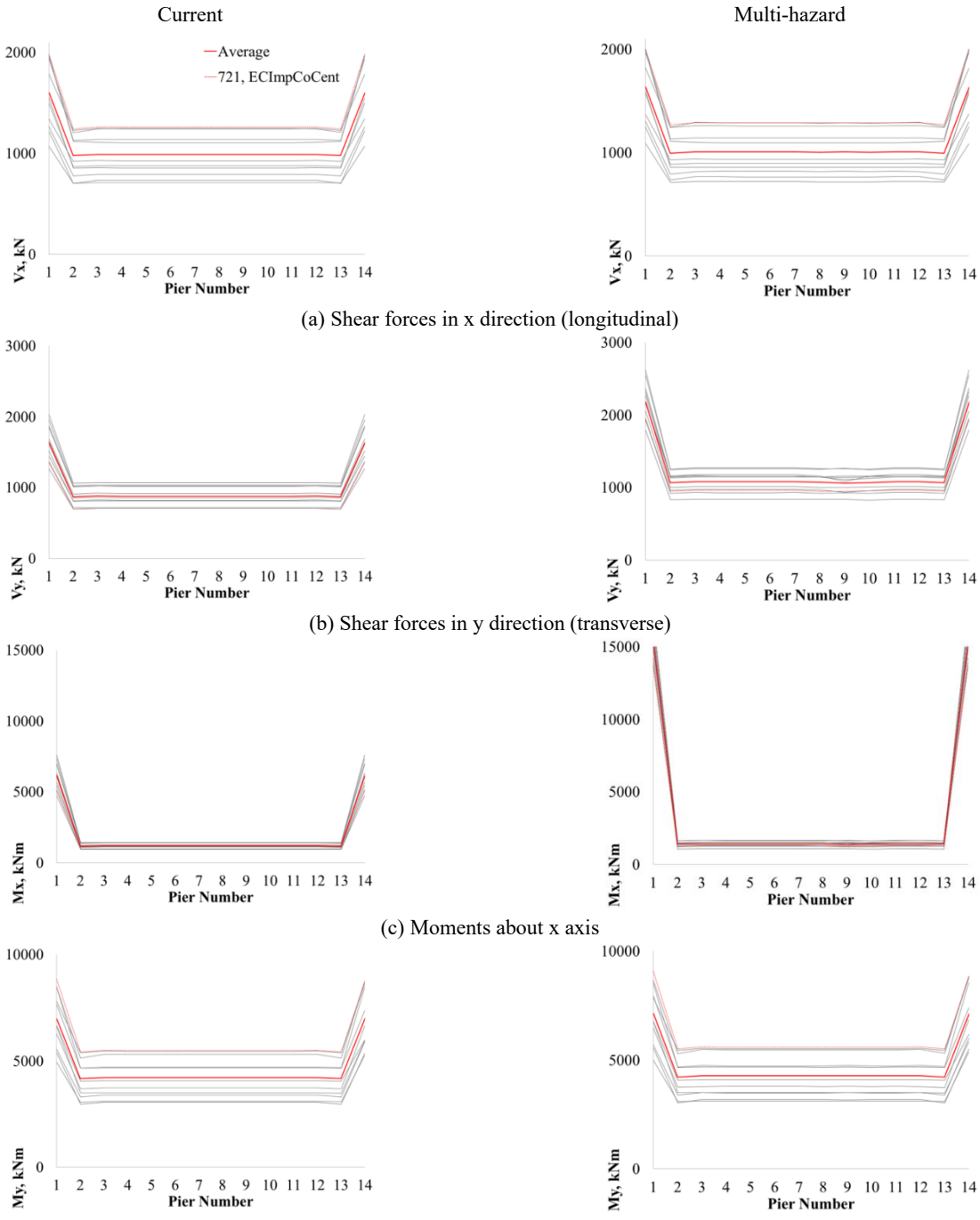

(a) Shear forces in x direction (longitudinal)

(b) Shear forces in y direction (transverse)

(c) Moments about x axis

(d) Moments about y axis

Fig. 13 The maximum pier column internal forces for current and multi-hazard conditions

strong axis) (M_x) were observed to approximately double from 7000 to 14000 kNm for the abutment shear walls (Fig. 13(c)).

For the piles, a high variation in internal forces was monitored with regard to the increase in scour depth for the multi-hazard condition (Figs. 14(a)-(d)). Herein, the internal forces augmented two to six fold due to the stiffness degradation in piles with the removal of the surrounding soil layers after scouring. This fact was the most significant for the shear forces in longitudinal direction of the bridge (V_x) (Fig. 14(a)). During seismic loading by means of THA, the lateral response of the bridge considering plastic hinge locations (Figs. 15(a)-(b)) and the hysteretic behavior of the selected bridge members (Figs. 16(a)-(d)) was monitored under the El Centro Imp. Co. Cent. ground motion record which was chosen arbitrarily among the ground motion suite. The plastic hinge rotation performance levels were tracked according to ASCE/SEI 41-17 (ASCE 2017) considering the rotation limits from A to E in which immediate occupancy (IO), life safety (LS), and collapse prevention (CP) limit states were defined as the acceptance criteria (Fig. 15(b)). As regard to the current condition, all pier columns were monitored to have rotation levels in between IO and LS beyond yielding, however the

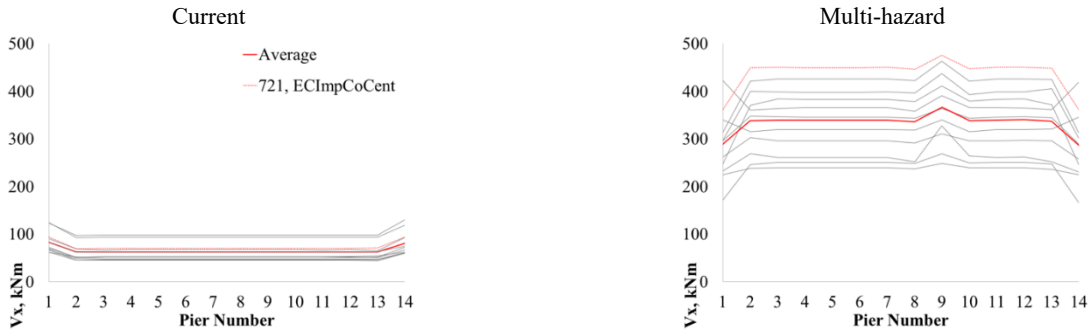

(a) Shear forces in x direction (longitudinal)

(b) Shear forces in y direction (transverse)

(c) Moments about x axis

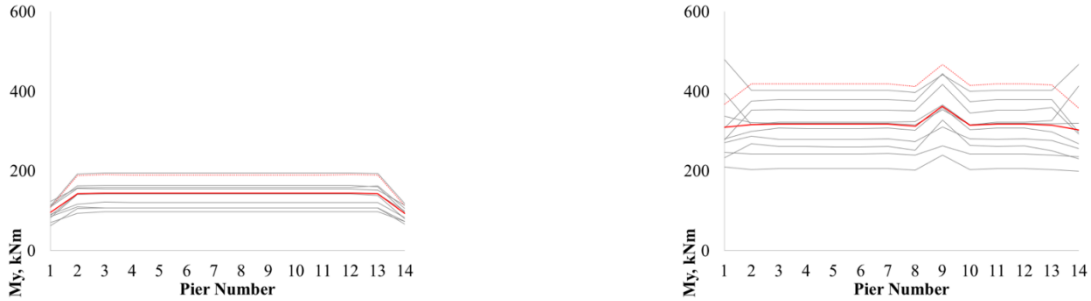

(d) Moments about y axis

Fig. 14 The maximum pile internal forces for current and multi-hazard conditions

abutments and the piles were shown to respond elastically (Fig. 15(a)). For the multi-hazard condition, in addition to the pier columns, some of the piles demonstrated inelastic response by plastic hinging with a lower rotation level between B and IO as compared to the pier columns (Fig. 15(b)). The abutment lateral response remained in the elastic region between A and B. In order to track rotation levels, the pier column and the pile located in Pier 2 (Figs. 15(a) and (b)) was selected for lateral response comparison in terms of hysteretic Moment – Rotation behavior (about longitudinal (x) and transverse (y) axes) under bidirectional lateral cycles due to the selected record (Figs. 16(a)-(d)). The lateral displacement, pier column internal force, and pile internal force variations for the selected members were presented (shown as the red star) with the selected ground motion record in Figs. 12-14, respectively. Regarding the moments about x axis, which designated the bridge behavior in the transverse direction, the pier column and the pile was shown to remain in the elastic range for the current condition, however minor plastic hinging was observed for the piles under the multi-hazard condition (Figs. 16(a)-(b)).

For the longitudinal response (i.e., moments about y axis), the pier column demonstrated inelastic behavior with considerable plastic rotation level while the pile exhibited elastic behavior under the current condition. However, under the multi-hazard condition, the pier column showed an inelastic response with a lower plastic rotation level as the pile was shown to enter the inelastic range with minor

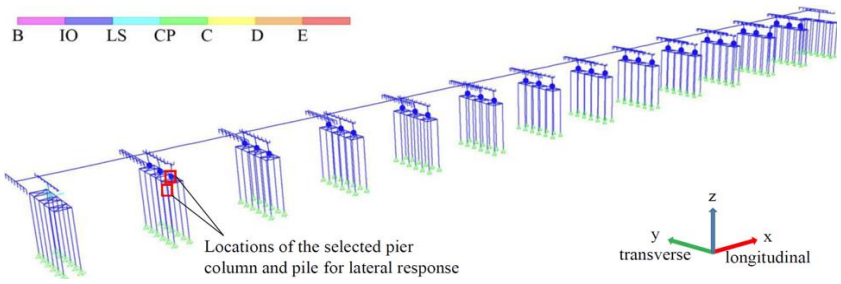

(a) Current

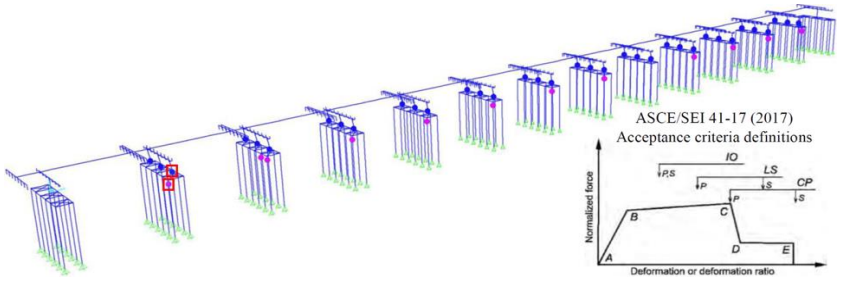

(b) Multi-hazard

Fig. 15 Plastic hinge distribution under El Centro Imp. Co. Cent. record

plastic hinging (Figs. 16(c)-(d)).

Consequently, in multi-hazard condition for the bridge with a higher scour depth, the seismic load and displacement demands were shown to migrate from the pier columns to the piles after scouring. This can be attributed to the fact that the internal forces that were shared by the pile and the surrounding soil in advance of scouring were solely resisted by the piles in the absence of soil after scouring. Thereby, it can be inferred that the internal forces that were previously resisted by the soil were transferred to the piles after scouring. This behavior gave rise to increasing levels of pile internal forces (Figs. 14(a)-(d)), consequently the rotations (Figs. 16(b) and (d)) and the lateral displacements (Figs. 12(a) and (b)) while keeping the pier column internal forces approximately constant (Figs. 13(a)-(d)). Besides, enhanced flexibility of piles after the removal of surrounding soil layers also led to an increase in lateral displacements. For the investigated bridge, due to the alignment of the columns such that their weak axis coincided with the bridge transverse axis, the lateral forces acting in the longitudinal direction led to plastic hinging in the pier columns instead of the pile group under current conditions (Figs. 15(a) and 16(c)). In addition, the lateral forces due to flood were resisted by the strong axis of the pier columns and the scoured pile group majorly resisted the flood loads after scouring while leading to a linear elastic response since the flood loads were observed to be insignificant regarding the pier column and pile group lateral load capacities. Therefore, it was ascertained that the scour substantially affected the behavior of laterally loaded piles and the interaction of bridge components and soil should be taken into consideration during bridge multi-hazard performance analyses.

4. Discussion

In this study an automated UAV based bridge multi-hazard assessment system was suggested for RC bridges crossing seasonal rivers under flood loading and earthquake excitations including the effects of scouring. The suggested method can be applied to only the bridges located on the rivers with dry river bed during most of the year since the UAV based measurement method was incapable of DEM construction in underwater regions. Thereby, the Boğaçay-II Bridge, which was constructed over Boğaçay in Antalya, Turkey, was selected as the case study. The current lateral seismic performance of the bridge was evaluated considering seasonal UAV measured scour depths. In order to predict the multi-hazard performance, the flood water depths were estimated after the HEC-RAS hydraulic analyses and the resultant flood induced scour depths were obtained. Afterward, bridge FEM was constituted automatically. Finally, after flood loading, nonlinear THA were carried out for evaluating the multi-hazard performance of the bridge with flood induced scour depths considering the lateral displacements, internal forces, and plastic rotations. In the light of obtained results; (a) scouring was shown to deteriorate the seismic behavior of the bridge. After scouring, the seismic internal force and displacement demands migrated from the pier columns to the piles. (b) Thus, the loss of lateral load capacity at bridge foundations may induce bridges to become highly vulnerable to failure when the effects of scour and earthquakes (i.e., THA) are combined. (c) The bridge members exhibit linear elastic response under flood loading even after scouring. Therefore, in the conducted study, an automated bridge multi-hazard evaluation system was proposed and its capabilities were verified. Further, future studies can be conducted on UAV-mounted bathymetric Lidar solutions to overcome the limitations of image-based measurements in underwater regions.

(a) Pier column response about x axis (longitudinal)

(b) Pile response about x axis (longitudinal)

(c) Pier column response about y axis (transverse)

(d) Pile response about y axis (transverse)

Fig. 16 Lateral response for the selected members under El Cent. Imp. Co. Cent. record

Acknowledgments

This work was supported by the Istanbul Technical University Scientific Research Project (ITU-BAP). Project No: MGA-2018-41393 and by the Akdeniz University Scientific Research Project (AU-BAP) Project No: FBA-2018-2877.

References

AASHTO (2014), AASHTO LRFD bridge design specifications, Transportation (Amst), American Association of State Highway and Transportation Officials, Inc.: Washington, D.C., USA.

AASHTO (2017), AASHTO LRFD Bridge Design Specifications, Washington, D.C., USA.

Alipour, A., Shafei, B. and Shinozuka, M. (2010), "Evaluation of uncertainties associated with design of highway bridges considering the effects of scouring and earthquake", *Proceedings of Structures Congress*, ASCE, Orlando, FL, USA, pp. 288-297.

ASCE (2016), ASCE/SEI 7-16, Minimum design loads and associated criteria for buildings and other structures, American Society of Civil Engineers, Reston, VA, USA. https://doi.org/10.1061/9780784412916

ASCE (2017), ASCE/SEI 41-17, Seismic evaluation and retrofit of existing buildings, American Society of Civil Engineers, Reston, VA, USA, 20191-4382.

Avsar, O., Atak, B. and Caner, A. (2017), "In-depth investigation of seismic vulnerability of an aging river bridge exposed to scour", *J. Perform. Constr. Facil.*, **31**(5). https://doi.org/10.1061/(ASCE)CF.1943-5509.0001036

Banerjee, S. and Prasad, G.G. (2013), "Seismic risk assessment of reinforced concrete bridges in flood-prone regions", *Struct. Infrastruct. Eng.*, **9**(9), 952-968. https://doi.org/10.1080/15732479.2011.649292

Cali, M. and Ambu, R. (2018), "Advanced 3D photogrammetric surface reconstruction of extensive objects by UAV camera image acquisition", *Sensors*, **18**(9), 2815. https://doi.org/10.3390/s18092815

Castillo, C., Perez, R., James, M.R., Quinton, J.N., Taguas, E.V. and Gomez, J.A. (2012), "Comparing the accuracy of several field methods for measuring gully erosion", *Soil Sci. Soc. Am. J.*, **76**(4), 1319-1332. https://doi.org/10.2136/sssaj2011.0390

Chen, S.Y., Laefer, D.F., Mangina, E., Zolanvari, S.M.I. and Byrne, J. (2019), "UAV bridge inspection through evaluated 3d reconstructions", *J. Bridge Eng.*, **24**(4). https://doi.org/10.1061/(ASCE)BE.1943-5592.0001343

Coveney, S. and Roberts, K. (2017), "Lightweight UAV digital elevation models and orthoimagery for environmental applications: data accuracy evaluation and potential for river flood risk modelling", *Int. J. Remote Sensing*, **38**(8-10), 3159-3180. https://doi.org/10.1080/01431161.2017.1292074

Czech, W., Radecki-Pawlik, A., Wyzga, B. and Hajdukiewicz, H. (2016), "Modelling the flooding capacity of a Polish Carpathian river: A comparison of constrained and free channel conditions", *Geom.*, **272**, 32-42. https://doi.org/10.1016/j.geomorph.2015.09.025

Deco, A. and Frangopol, D.M. (2011), "Risk assessment of highway bridges under multiple hazards", *J. Risk Res.*, **14**(9), 1057-1089. https://doi.org/10.1080/13669877.2011.571789

Dorafshan, S. and Maguire, M. (2018), "Bridge inspection: human performance, unmanned aerial systems and automation", *J. Civil Struct. Health Monitor.*, **8**(3), 443-476. https://doi.org/10.1007/s13349-018-0285-4

Duque, L., Seo, J. and Wacker, J. (2018), "Bridge deterioration quantification protocol using UAV", *J. Bridge Eng.*, **23**(10). https://doi.org/10.1061/(ASCE)BE.1943-5592.0001289

Ellenberg, A., Kontsos, A., Moon, F. and Bartoli, I. (2016), "Bridge deck delamination identification from unmanned aerial vehicle infrared imagery", *Automat. Constr.*, **72**, 155-165. https://doi.org/10.1016/j.autcon.2016.08.024

Escobar-Wolf, R., Oommen, T., Brooks, C.N., Dobson, R.J. and Ahlborn, T.M. (2018), "Unmanned Aerial Vehicle (UAV)-based assessment of concrete bridge deck delamination using thermal and visible camera sensors: a preliminary analysis", *Res. Nondestruct. Eval.*, **29**(4), 183-198. https://doi.org/10.1080/09349847.2017.1304597

FHWA (2009), Federal Highway Administration "HY-8 Software – Hydraulics Engineering" online access at; http://www.fhwa.dot.gov/engineering/hydraulics/software/hy8

Fioklou, A. and Alipour, A. (2019), "Significance of non-uniform scour on the seismic performance of bridges", *Struct. Infrastruct. Eng.*, **15**(6), 822-836. https://doi.org/10.1080/15732479.2019.1584226

Flener, C., Vaaja, M., Jaakkola, A., Krooks, A., Kaartinen, H., Kukko, A., Kasvi, E., Hyyppa, H., Hyyppa, J. and Alho, P. (2013), "Seamless mapping of river channels at high resolution using mobile lidar and UAV-photography", *Remote Sensing*, **5**(12), 6382-6407. https://doi.org/10.3390/rs5126382

Gehl, P. and D'Ayala, D. (2016), "Development of bayesian networks for the multi-hazard fragility assessment of bridge systems", *Struct. Safety*, **60**, 37-46. https://doi.org/10.1016/j.strusafe.2016.01.006

Gidaris, I., Padgett, J.E., Barbosa, A.R., Chen, S.R., Cox, D., Webb, B. and Cerato, A. (2017), "Multiple-hazard fragility and restoration models of highway bridges for regional risk and resilience assessment in the United States: state-of-the-art review", *J. Struct. Eng.*, **143**(3). https://doi.org/10.1061/(ASCE)ST.1943-541X.0001672

Goncalves, P., Marafuz, I. and Gomes, A. (2015), "Flood hazard, Santa Cruz do Bispo Sector, Leca River, Portugal: a methodological contribution to improve land use planning", *J. Maps*, **11**(5), 760-771. https://doi.org/10.1080/17445647.2014.974226

Guo, X., Badroddin, M. and Chen, Z.Q. (2019), "Scour-dependent empirical fragility modelling of bridge structures under earthquakes", *Adv. Struct. Eng.*, **22**(6), 1384-1398. https://doi.org/10.1177/1369433218815433

Hackl, J., Adey, B.T., Wozniak, M. and Schumperlin, O. (2018), "Use of unmanned aerial vehicle photogrammetry to obtain topographical information to improve bridge risk assessment", *J. Infrastruct. Syst.*, **24**(1). https://doi.org/10.1061/(ASCE)IS.1943-555X.0000393

Hada, Y., Nakao, M., Yamada, M., Kobayashi, H., Sawasaki, N., Yokoji, K., Kanai, S., Tanaka, F., Date, H., Pathak, S., Yamashita, A., Yamada, M. and Sugawara, T. (2017), "Development of a bridge inspection support system using two-wheeled multicopter and 3d modeling technology", *J. Dis. Res.*, **12**(3), 593-606. https://doi.org/10.20965/jdr.2017.p0593

Hemmelder, S., Marra, W., Markies, H. and De Jong, S.M. (2018), "Monitoring river morphology & bank erosion using UAV imagery - A case study of the river Buech, Hautes-Alpes, France", *Int. J. Appl. Earth Observ. Geoinform.*, **73**, 428-437. https://doi.org/10.1016/j.jag.2018.07.016

Hoskere, V., Park, J.W., Yoon, H. and Spencer, B.F. (2019), "Vision-based modal survey of civil infrastructure using unmanned aerial vehicles", *J. Struct. Eng.*, **145**(7). https://doi.org/10.1061/(ASCE)ST.1943-541X.0002321

Hu, X.Y., Wang, B.W. and Ji, H. (2013), "A wireless sensor network-based structural health monitoring system for highway bridges", *Comput.-Aided Civil Infr. Eng.*, **28**(3), 193-209. https://doi.org/10.1111/j.1467-8667.2012.00781.x

Hung, C.C. and Yau, W.G. (2017), "Vulnerability evaluation of scoured bridges under floods", *Eng. Struct.*, **132**, 288-299. https://doi.org/10.1016/j.engstruct.2016.11.044

Ikeda, T., Minamiyama, S., Yasui, S., Ohara, K., Ichikawa, A., Ashizawa, S., Okino, A., Oomichi, T. and Fukuda, T. (2019), "Stable camera position control of unmanned aerial vehicle with three-degree-of-freedom manipulator for visual test of bridge inspection", *J. Field Robotics*, **36**(7), 1212-1221. https://doi.org/10.1002/rob.21899

Izumida, A., Uchiyama, S. and Sugai, T. (2017), "Application of UAV-SfM photogrammetry and aerial lidar to a disastrous flood: repeated topographic measurement of a newly formed crevasse splay of the Kinu River, central Japan", *Natural Hazards Earth Syst. Sci.*, **17**(9), 1505-1519. https://doi.org/10.5194/nhess-17-1505-2017

James, M.R. and Robson, S. (2012), "Straightforward reconstruction of 3D surfaces and topography with a camera: Accuracy and geoscience application", *J. Geophys. Res.-Earth Surface*, **117**. https://doi.org/10.1029/2011JF002289

Javernick, L., Brasington, J. and Caruso, B. (2014), "Modeling the topography of shallow braided rivers using Structure-from-Motion photogrammetry", *Geomorphology*, **213**, 166-182. https://doi.org/10.1016/j.geomorph.2014.01.006

Jung, H.J., Lee, J.H., Yoon, S. and Kim, I.H. (2019), "Bridge inspection and condition assessment using Unmanned Aerial Vehicles (UAVs): Major challenges and solutions from a practical perspective", *Smart Struct. Syst., Int. J.*, **24**(5), 669-681. https://doi.org/10.12989/sss.2019.24.5.669

Khaloo, A., Lattanzi, D., Cunningham, K., Dell'Andrea, R. and

Riley, M. (2018), "Unmanned aerial vehicle inspection of the Placer River Trail Bridge through image-based 3D modelling", *Struct. Infrastruct. Eng.*, **14**(1), 124-136. https://doi.org/10.1080/15732479.2017.1330891

Kim, I.H., Jeon, H., Baek, S.C., Hong, W.H. and Jung, H.J. (2018), "Application of crack identification techniques for an aging concrete bridge inspection using an UAV", *Sensors*, **18**(6), 1881. https://doi.org/10.3390/s18061881

Kizilduman, H.S. (2016), "A Study on Seismic Behavior of Scour-Vulnerable Bridges", Civil Engineering, Middle East Technical University, Turkey.

Kizilduman, H.S., Yanmaz, A.M. and Caner, A. (2018), "Stability of bridge piers subjected to a probable flood event followed by a probable seismic event", *J. Perf. Constr. Facil.*, **32**(1). https://doi.org/10.1061/(ASCE)CF.1943-5509.0001123

Klinga, J.V. and Alipour, A. (2015), "Assessment of structural integrity of bridges under extreme scour conditions", *Eng. Struct.*, **82**, 55-71. https://doi.org/10.1016/j.engstruct.2014.07.021

Lagasse P.F., Schall J.D. and Price, G.R. (1997), *Instrumentation for Measuring Scour at Bridge Piers and Abutments*, NCHRP Report no. 396, Transportation Research Board, Washington, D.C., USA.

Langhammer, J. (2018), "UAV monitoring of stream restorations", *Hydrology*, **6**(2), 29. https://doi.org/10.3390/hydrology6020029

Lee, J.K., Kim, J.O. and Park, S.J. (2019), "A study on the UAV image-based efficiency improvement of bridge maintenance and inspection", *J. Intel. Fuzzy Syst.*, **36**(2), 967-983. https://doi.org/10.3233/JIFS-169873

Lei, B., Wang, N., Xu, P.C. and Song, G.B. (2018), "New crack detection method for bridge inspection using UAV incorporating image processing", *J. Aerosp. Eng.*, **31**(5). https://doi.org/10.1061/(ASCE)AS.1943-5525.0000879

Liao, K.W., Kung W.C. and Chen, J.W. (2018a), "Probabilistic safety evaluation of a river bridge substructure against floods", *Proceedings of the Institution of Civil Engineers-Structures and Buildings*, **171**(7), 517-527.

Liao, K.W., Muto, Y. and Gitomarsono, J. (2018b), "Reliability analysis of river bridge against scours and earthquakes", *J. Perform. Constr. Facil.*, **32**(3).

Liu, P., Chen, A.Y., Huang, Y.N., Han, J.Y., Lai, J.S., Kang, S.C., Wu, T.H., Wen, M.C. and Tsai, M.H. (2014), "A review of rotorcraft Unmanned Aerial Vehicle (UAV) developments and applications in civil engineering", *Smart Struct. Syst., Int. J.*, **13**(6), 1065-1094. https://doi.org/10.12989/sss.2014.13.6.1065

McVay, M.C. and Niraula, L. (2004), "Development of modified T-Z curves for large diameter piles/drilled shafts in limestone for FBPier", Rep. No. 4910-4504-878-12, Nat. Tech. Inf. Serv., Springfield.

Metni, N. and Hamel, T.A. (2007), "A UAV for bridge inspection: Visual servoing control law with orientation limits", *Automat. Constr.*, **17**(1), 3-10. https://doi.org/10.1016/j.autcon.2006.12.010

Muthusamy, M., Casado, M.R., Salmoral, G., Irvine, T. and Leinster, P. (2019), "A RS based integrated approach to quantify the impact of fluvial and pluvial flooding in an urban catchment", *Rem. Sens.*, **11**(5).

Niraula, L.D. (2004) "Development of Modified T-z Curves for Large Diameter Piles/Drilled Shafts in Limestone for FB Pier.", Master Thesis, University of Florida, USA.

Omar, T. and Nehdi, M.L. (2017), "Remote sensing of concrete bridge decks using unmanned aerial vehicle infrared thermography", *Automat. Constr.*, **83,** 360-371. https://doi.org/10.1016/j.autcon.2017.06.024

Ozcan, O. and Musaoglu, N. (2017), "Intercomparison of satellite precipitation with gauge data using point frequency analysis", *Ipsi Bgd Transact. Internet Res.*, **13**(2).

Ozcan, O. and Ozcan, O. (2018), "Multi-hazard assessment of rc bridges using unmanned aerial vehicle-based measurements", *Baltic J. Road Bridge Eng.*, **13**(3), 192-208. https://doi.org/10.7250/bjrbe.2018-13.412

Ozcan, O. and Ozcan, O. (2019), "Effect of hydrogeo-morphological changes in flood plain on bridge multi-hazard performance", *Fresenius Environ. Bull.*, **28**(2), 956-962.

Pan, Y., Dong, Y.Q., Wang, D.L., Chen, A.R. and Ye, Z. (2019), "3-D reconstruction of structural surface model of heritage bridges using UAV-based photogrammetric point clouds", *Remote Sensing*, **11**(10).

Patel, D.P., Ramirez, J.A., Srivastava, P.K., Bray, M. and Han, D.W. (2017), "Assessment of flood inundation mapping of Surat city by coupled 1D/2D hydrodynamic modeling", *Natural Hazards*, **89**(1), 93-130. https://doi.org/10.1007/s11069-017-2956-6

PEER (2015), Pacific Earthquake Engineering Research Center – PEER. Ground motion database.

Reese, L.C., Cox, W.R. and Koop, F.D. (1974), "Field testing and analysis of laterally loaded piles in sand", *Proceedings of the VI Annual Offshore Technology Conference*, Houston, TX, USA, 2(OTC 2080), pp, 473-485.

Richardson, E.V., Harrison, L.J., Richardson, J.R. and Davis, S.R. (1993), *Evaluating Scour at Bridges - HEC-18*, FHWA Report, FHWA-IP-90-017, Washington, D.C., USA.

Salaan, C.J.O., Okada, Y., Mizutani, S., Ishii, T., Koura, K., Ohno, K. and Tadokoro, S. (2018), "Close visual bridge inspection using a UAV with a passive rotating spherical shell", *J. Field Robotics*, **35**(6), 850-867. https://doi.org/10.1002/rob.21781

Sanchez-Cuevas, P.J., Ramon-Soria, P., Arrue, B., Ollero, A. and Heredia, G. (2019), "Robotic system for inspection by contact of bridge beams using UAVs", *Sensors*, **19**(2), 305. https://doi.org/10.3390/s19020305

SAP2000 v18 (2018), Integrated Finite Element Analysis and Design of Structures Software, Berkeley, CA, USA.

Schumann, G.J.P., Muhlhausen, J. and Andreadis, K.M. (2019), "Rapid mapping of small-scale river-floodplain environments using UAV SfM supports classical theory", *Remote Sensing*, **11**(8), 982. https://doi.org/10.3390/rs11080982

Seo, J., Duque, L. and Wacker, J. (2018), "Drone-enabled bridge inspection methodology and application", *Automat. Constr.*, **94**, 112-126. https://doi.org/10.1016/j.autcon.2018.06.006

SHWR (2018), Bogacay Project Evaluation Report, Antalya, Turkey, 2018, pp.112. [In Turkish]

Skibniewski, M., Tserng, H.P., Ju, S.H., Feng, C.W., Lin, C.T., Han, J.Y., Weng, K.W. and Hsu, S.C. (2014), "Web-based real time bridge scour monitoring system for disaster management", *Baltic J. Road Bridge Eng.*, **9**(1), 17-25. https://doi.org/10.3846/bjrbe.2014.03

Song, S.T., Wang, C.Y. and Huang, W.H. (2015), "Earthquake damage potential and critical scour depth of bridges exposed to flood and seismic hazards under lateral seismic loads", *Earthq. Eng. Eng. Vib.*, **14**(4), 579-594. https://doi.org/10.1007/s11803-015-0047-9

TEC (2018), Turkey Building Earthquake Code, Ankara, Turkey.

Villanueva, J.R.E., Martinez, L.I. and Montiel, J.I.P. (2019), "DEM generation from fixed-wing uav imaging and lidar-derived ground control points for flood estimations", *Sensors*, **19**(14), 3205. https://doi.org/10.3390/s19143205

Wang, S.C., Liu, K.Y., Chen, C.H. and Chang, K.C. (2015), "Experimental investigation on seismic behavior of scoured bridge pier with pile foundation", *Earthq. Eng. Struct. Dyn.*, **44**(6), 849-864. https://doi.org/10.1002/eqe.2489

Wang, S.T. and Reese, L.C. (1993), "COM624P – Laterally loaded pile analysis program for the microcomputer", version 2.0, Federal Highway Administration Publication No. FHWA-SA-

91-048.
Wang, Z.H., Duenas-Osorio, L. and Padgett, J.E. (2014), "Influence of scour effects on the seismic response of reinforced concrete bridges", *Eng. Struct.*, **76**, 202-214. https://doi.org/10.1016/j.engstruct.2014.06.026
Wardhana, K. and Hadipriono, F.C. (2003), "Analysis of recent bridge failures in the United States", *J. Perform. Constr Facil.*, **17**(3), 144-150. https://doi.org/10.1061/(ASCE)0887-3828(2003)17:3(144)
Watanabe, Y. and Kawahara, Y. (2016), "UAV photogrammetry for monitoring changes in river topography and vegetation", *Proceedings of the 12th International Conference on Hydroinformatics*, Volume 154, pp. 317-325.
Wilheit, T. (2003), *The TRMM Measuring Concept*, *In Cloud Systems*, *Hurricanes*, *and the TRMM*, *Meteorological Monographs*, American Meteorological Society, Boston, MA, USA.
Yanmaz, A.M. and Caner, A. (2012), "Comments on the Failure of Caycuma Bridge", Turkish Association for Bridge and Structural Engineering, Ankara, Turkey. [In Turkish]
Yilmaz, T., Banerjee, S. and Johnson, P.A. (2018), "Uncertainty in risk of highway bridges assessed for integrated seismic and flood hazards", *Struct. Infrastruct. Eng.*, **14**(9), 1182-1196. https://doi.org/10.1080/15732479.2017.1402065
Zaky, A., Özcan, O. and Avşar, Ö. (2020), "Seismic failure analysis of concrete bridges exposed to scour", *Eng. Fail. Anal.*, **115**, 104617. https://doi.org/10.1016/j.engfailanal.2020.104617

HJ